Low-Temperature Ion-Exchange Synthesis of Layered $LiNiO_2$ Single Crystals with High Ordering

Leonhard Karger,[a] Daniel Weber,[a,b]* Damian Goonetilleke,[a] Andrey Mazilkin,[a] Hang Li,[b] Ruizhuo Zhang,[a] Yuan Ma,[a] Sylvio Indris,[b,c] Aleksandr Kondrakov,[a,d] Jürgen Janek,[a,e]* and Torsten Brezesinski[a]*

[a] Battery and Electrochemistry Laboratory (BELLA), Institute of Nanotechnology, Karlsruhe Institute of Technology (KIT), Herrmann-von-Helmholtz-Platz 1, 76344 Eggenstein-Leopoldshafen, Germany.

[b] Institute for Applied Materials-Energy Storage Systems (IAM-ESS), Karlsruhe Institute of Technology (KIT), Herrmann-von-Helmholtz-Platz 1, 76344 Eggenstein-Leopoldshafen, Germany.

[c] Helmholtz Institute Ulm (HIU) Electrochemical Energy Storage, Helmholtzstr. 11, 89081 Ulm, Germany.

[d] BASF SE, Carl-Bosch-Str. 38, 67056 Ludwigshafen, Germany.

[e] Institute of Physical Chemistry & Center for Materials Research (ZfM/LaMa), Justus-Liebig-University Giessen, Heinrich-Buff-Ring 17, 35392 Giessen, Germany.

Abstract

Layered Ni-rich oxide cathode materials are being explored in an effort to boost the energy density of lithium-ion batteries, especially for automotive applications. Among them, the ternary phase $LiNiO_2$ (LNO) is a promising candidate, but brings along various issues, such as poor structural stability. The material is prone to disordering (Li off-stoichiometry) when prepared by conventional solid-state synthesis, leading to the presence of Ni^{2+} in the Li layer. These point defects negatively affect the utilization of the Li inventory, thereby limiting the practical specific capacity. In this work, we report on a two-step synthesis approach that avoids the formation of nickel substitutional defects. First, $NaNiO_2$ (NNO) is prepared, showing no such defects due to larger differences in ionic radii between Ni^{2+}/Ni^{3+} and Na^+. NNO is then subjected to Na^+/Li^+ exchange under mild conditions. In so doing, monolithic LNO particles free of $Ni_{Li}^{\bullet}$ defects can be produced at relatively low temperatures. Notably, this route allows for tailoring of the grain size, a strategy that may be used to gain insights into the structure-size-property relations in single-crystalline LNO.

Keywords

Lithium-ion battery, cathode active material, low-temperature synthesis, single crystal, size tailoring, layering

Introduction

Cathode active materials (CAMs) from the $LiNi_xCo_yMn_zO_2$ (NCM) and $LiNi_xCo_yAl_zO_2$ (NCA) material families (solid solutions based on layered ternary compounds) have been widely employed in commercial high energy density Li-ion batteries (LIBs).[1,2] In an effort to boost the specific energy, compositions with increasing Ni content have been adopted. The substitution of cobalt with nickel is also desirable owing to its higher abundance and lower cost while retaining high theoretical specific capacity. However, increasing the Ni content [i.e. development of so-called Ni-rich CAMs (>80% Ni) and especially $LiNiO_2$ (LNO)] has been linked to lower cycling stability. The latter is usually attributed to unfavorable structural transitions at high levels of delithiation (high states of charge).[3,4] Nickel substitutional defects on the Li site ($Ni_{Li}^{\bullet}$) represent another detrimental factor kinetically hindering the occupation of neighboring Li sites during discharge.

LNO adopts a rhombohedral structure with space group $R\bar{3}m$, in which ideally Li^+ and Ni^{3+} cations separate into different layers within a cubic close-packed lattice of O^{2-} anions. When prepared by solid-state synthesis, $Ni_{Li}^{\bullet}$ defects (Ni^{2+} ions present on the crystallographic Li site) are formed. These defects may originate from incomplete transition of the cubic, 3D-isotropic $Ni_{1-x}Li_xO_{1-\delta}$ intermediate[5,6] into the layered, anisotropic 2D-type structure of LNO, due to Li off-stoichiometry and/or insufficient oxygen activity.[7] Experimentally, the oxidation of Ni^{2+} from the reactant to Ni^{3+} requires high temperatures of at least 600 °C for kinetic reasons, which typically leads to lithium losses (LiOH is commonly used as Li precursor).[8] This competition between minimum temperature and lithium loss is inherent to the solid-state synthesis of LNO,[9] with even the least defective samples having more than 1 to 2% of Ni^{2+} on the Li site.[10] This is related to the similar ionic radii of Ni^{2+} (r = 0.69 Å) and Li^+ (r = 0.76 Å), and thus reduced driving force for oxidation and separation into discrete Ni^{3+} and Li^+ layers.[11]

Because the point defects affect the material properties, especially the electrochemical behavior, various characterization techniques have been utilized for the study of Li off-stoichiometry in LNO, including X-ray diffraction (XRD), magnetometry, magic-angle spinning nuclear magnetic resonance (MAS NMR) spectroscopy, and empiric correlations (e.g. voltage range at which characteristic phase transitions occur).[10,12–14] Doping with Mg^{2+}, for example, has been investigated as a means to decrease off-stoichiometry, yet the effects observed can also be interpreted via complex substitution patterns.[15,16] Despite this toolbox, full suppression of Li off-stoichiometry remains elusive in LNO synthesized at elevated temperatures, and thorough defect analysis is experimentally very challenging.[10,17,18]

Another approach toward electrochemically active LNO with low point-defect concentration relies on low-temperature and/or ion-exchange reactions, generally aiming at the exchange of H^+ for Li^+ in NiOOH. When NiOOH and $LiOH{\cdot}H_2O$ react under hydrothermal or low-temperature (<200 °C) conditions, as reported by Tarascon and coworkers,[19–21] the resulting LNO delivers a specific charge capacity of

q_{ch} ≈ 120 mAh g^{-1}, much lower than the theoretical one (q_{th} = 275 mAh g^{-1}). The decreased capacity originates from the presence of NiOOH and NiO impurity phases, which have been shown to form as decomposition products in water.[22,23] Consequently, water-based synthesis appears less suited for the preparation of high-capacity LNO. In an alternative route, LNO was produced from NiOOH and LiOH·H_2O in the temperature range from 450 to 600 °C by Sun *et al*. The material obtained at 550 °C delivered specific charge and discharge capacities of q_{ch} ≈ 183 mAh g^{-1} and q_{dis} ≈ 170 mAh g^{-1}, respectively, falling short of achieving the goal of >200 mAh g^{-1} that can be expected for LNO made from solid-state reaction.[24] While these investigations focused on the exchange of the smaller H^+ for Li^+, a parent material having a larger monovalent cation might be capable of more readily establishing layers as structural motif. One such example is $NaNiO_2$ (NNO), a material that crystallizes in the space group $C2/m$ and exhibits well separated layers of Na^+ and Ni^{3+}.[25] NNO is typically made from NiO and Na_2O_2 or Na_2O at elevated temperatures under oxidizing conditions[25–28] for studying its magnetic and electrochemical properties.[29–33] Because of the large size difference between Na^+ (r = 1.02 Å) and Ni^{2+}/Ni^{3+} (r(Ni^{2+}) = 0.69 Å, r(Ni^{3+}) = 0.56 Å), they separate well into different layers, without formation of interlayer occupancy defects. Overall, NNO represents an attractive parent compound for topotactic ion exchange (Na^+ vs. Li^+), which has already been demonstrated for other layered materials.[34–42]

Herein, we examine the synthesis of LNO with high ordering by means of ion exchange from NNO for application in LIB cells. Monolithic material is prepared from commercially available polycrystalline $Ni(OH)_2$ and NaOH in the first step. These reactants allow for control over grain size by varying the annealing temperature. In a second step, Na^+ is exchanged for Li^+ in molten $LiNO_3$ at temperatures below the formation temperature of $Ni_{Li}^{\bullet}$ defects. The structural and electrochemical results indicate the absence of Ni^{2+} substitutional defects in the interlayer space of the single-crystalline LNO CAM.

Results and Discussion

$NaNiO_2$ Synthesis

NNO was prepared from polycrystalline $Ni(OH)_2$ and NaOH by heating powder mixtures at temperatures between 450 and 700 °C under O_2 gas flow for 6 to 12 h, as described in the Experimental section. The corresponding samples are referred to as NNO-ϑ. The observed XRD reflections match those of single-phase NNO (see **Figure S1**). Elemental analysis confirms the expected composition, but points to the presence of an amorphous, Na^+-rich side phase, which is likely residual NaOH (see **Table S1**). Calcination at temperatures lower than 450 °C or higher than 750 °C yields a material with a rocksalt-type phase, in addition to layered NNO. Rietveld refinement analysis was performed based on a model of the NNO structure in the $C2/m$ space group with lattice parameters of a ≈ 5.32 Å, b ≈ 2.84 Å, c ≈ 5.58 Å, and β ≈ 110.4°. The refined parameters agree with those reported in the literature and of a reference sample

synthesized by solid-state reaction from Na_2O_2 and NiO (see Supporting Information for experimental details).[31] The lattice parameters are shown in **Table 1**. Models assuming the presence of Ni^{2+} on the interlayer Na site were tested too. However, the fraction of $Ni_{Na}^{\bullet}$ converged to zero in the refinements. Accordingly, NNO prepared from $Ni(OH)_2$ and NaOH consists of well separated layers of sodium and nickel and appears to be free of substitutional defects.

Table 1. Rietveld refinement results for reference NNO and samples prepared from $Ni(OH)_2$ and NaOH at temperatures of 450 °C (6 h), 600 °C (6 h and 12 h*), and 700 °C (6 h).

Material	*a* [Å]	*b* [Å]	*c* [Å]	*β* [°]	*V* [Å^3]	R_{Bragg} [%]
Ref. NNO	5.3187(1)	2.8428(1)	5.5790(1)	110.449(1)	79.040(3)	2.91
NNO-450	5.3140(2)	2.8421(1)	5.5770(2)	110.441(2)	78.924(5)	3.12
NNO-600	5.3158(1)	2.8419(1)	5.5779(2)	110.482(2)	78.938(5)	3.19
NNO-600*	5.3183(1)	2.8432(1)	5.5796(1)	110.474(1)	79.041(3)	2.36
NNO-700	5.3173(2)	2.8424(1)	5.5789(1)	110.485(1)	78.987(3)	2.67

Synthesis of $LiNiO_2$ from $NaNiO_2$ via Ion Exchange

The exchange of Na^+ for Li^+ ions was studied in some detail for NNO-600 heated for 12 h in O_2 atmosphere (see XRD patterns and electron microscopy images in **Figure 1a**-**f**) using a 20 mol % excess of molten $LiNO_3$ as lithium source. The product (IE-LNO) was washed repeatedly with deionized water and finally vacuum dried. XRD (see **Figures 1f** and **S1**) suggests that the material is single phase. However, elemental analysis revealed the presence of residual sodium at about 10% (see **Table S1**). From the absence of additional reflections, we conclude that a significant fraction of Na^+ resides in the IE-LNO structure.

As the described route requires an aqueous washing step that is known to be detrimental to the LNO (surface structure and constitution), alternative reaction pathways were examined too. However, all other solvents and low-melting Li salts tested for $LiNO_3$ removal and ion exchange, respectively, partially or violently reacted with the LNO and/or NNO (see Supporting Information for details). Overall, the ion-exchange reaction with $LiNO_3$ yielded the most promising results. Additionally, reference LNO was prepared by conventional solid-state synthesis (SS-LNO) at 700 °C, following the description provided in the Supporting Information.

Both IE-LNO and SS-LNO crystallize in the $R\bar{3}m$ space group, and the refined structural parameters are in agreement with literature data (see **Tables 2** and **S2**). Although the XRD pattern collected from the IE-LNO CAM indicates structural similarity to SS-LNO, subtle differences can be observed. Except for 003, all other reflections are broadened. This is likely due to strain introduced by the residual Na^+ ions. There

are also distinct differences in lattice parameter-derived variables used to characterize the degree of layering and the $Ni_{Li}^{\bullet}$ defect concentration in LNO, namely the *c*/*a* ratio and unit cell volume. For $Li_{1-z}Ni_{1+z}O_2$ with z = 0.38, the *c*/*a* ratio equals 4.899 and increases toward 4.95 with decreasing z, while $V \approx 104.1$ Å^3 and decreases toward 101.5(1) Å^3 with $z \rightarrow 0$.[10] For SS-LNO, these metrics agree well with the literature for low-*z* LNO within the experimental error (*c*/*a* = 4.937, V = 101.420(3) Å^3). For IE-LNO, on the other hand, the *c*/*a* ratio (4.940) is slightly higher than that of SS-LNO, indicating some improvement in the degree of layering and low cation disorder. However, this is in contrast to the larger unit cell volume (V = 101.634(9) Å^3) found for IE-LNO, suggesting an increased amount of substitutional defects. The deviation from the known correlations can be rationalized by the presence of Na_{Li}^{x} rather than $Ni_{Li}^{\bullet}$. In the case of Li off-stoichiometry (deficiency), Ni_{Ni}' defects are generated for charge compensation. This leads to an increase in unit cell volume, since Ni^{2+} is larger in size than Ni^{3+}. The *c*/*a* ratio in turn decreases (increase in lattice parameter *a*). By contrast, no charge compensation is required upon Na_{Li}^{x} formation, leading to the observation of increased unit cell volume. The latter is enhanced by the larger size of Na^+ compared to Ni^{2+} while maintaining a high *c*/*a* ratio.[11] For NNO, both the unit cell volume (with $V' = 3/2 \cdot V_m \approx 118.6$ Å^3) and pseudohexagonal *c*'/*a*' ratio (with $c'/a' = 3 \cdot c_m \cdot \sin\beta / (1/2 \cdot (a_m^2 + b_m^2)^{1/2})) \approx 5.201$) are larger compared to LNO. In addition, Rietveld refinement indicates the presence of electron density on the crystallographic site of lithium for both IE- and SS-LNO. This electron density can be refined to 1.7(2)% $Ni_{Li}^{\bullet}$ for SS-LNO. For IE-LNO, it can be either interpreted as 5.0(8)% Na_{Li}^{x} or 1.6(2)% $Ni_{Li}^{\bullet}$. Based on the above results, we assign the excess electron density to Na_{Li}^{x} point defects. According to previous studies, the solubility limit of Na^+ is ≤5% relative to lithium.[25,43] This is consistent with our refinement data. It should be noted that Na-doped SS-LNO reported in the literature and reference samples prepared in the present work (see Supporting Information for experimental details and **Figure S2**) show cycling behaviors similar to undoped LNO.[25,43] We therefore assume that the residual sodium in the IE-LNO CAM has no major effect on the electrochemical properties. Minor differences in structural parameters were found for a sample that was subjected to a second ion-exchange step (see **Table S2**). While helping to slightly decrease the Na_{Li}^{x} defect concentration, this approach was not pursued further considering the detrimental effect of washing.

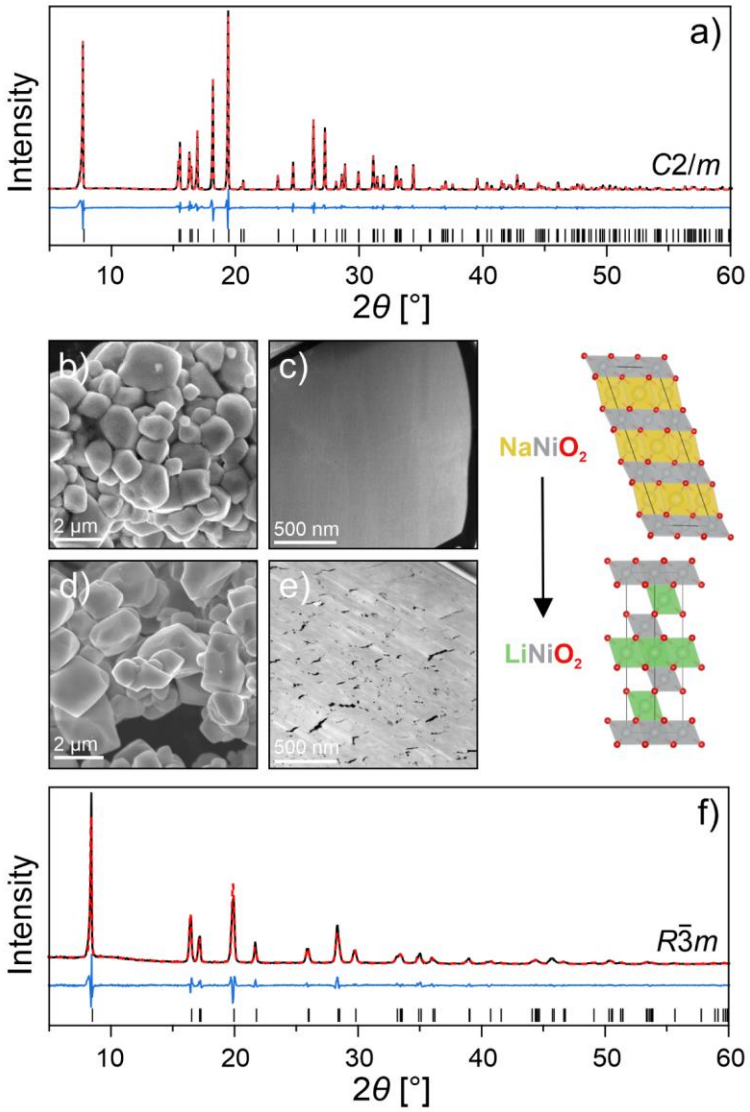

Figure 1. a, f) XRD pattern and corresponding Rietveld refinement profile for NNO-600 and IE-LNO, respectively. b, d) SEM images and c, e) FIB-cut STEM images. Schematic structures of the unit cell for $NaNiO_2$ and $LiNiO_2$ are shown on the right.

Table 2. Rietveld refinement results for water-washed IE-LNO and SS-LNO.

Material	*a* [Å]	*c* [Å]	*V* [Å^3]	Substitutional defects [%]	R_{Bragg} [%]
SS-LNO	2.8732(3)	14.1853(3)	101.420(3)	1.7(2) Ni_{Li}	1.83
IE-LNO	2.8748(2)	14.2001(2)	101.634(9)	5.0(8) Na_{Li}	1.75

^{7}Li and ^{23}Na MAS NMR Spectroscopy

^{7}Li MAS NMR spectroscopy measurements were conducted on the IE-LNO sample for probing both the local Li^+ environment and the presence of Ni^{2+} (S = 1) in the Li layer. The data were compared to NMR results obtained on a series of $Li_{1-z}Ni_{1+z}O_2$ CAMs

(referred to as LNO-set1), for which *z* was varied from about 0.03 to 0.08 by using different amounts of $LiOH \cdot H_2O$ in the synthesis [*n*(Ni):*n*(Li) = 1:(0.95 - 1.05)]. The measured NMR spectra are shown in **Figure 2a**. For all samples, the main peak is observed at 704 - 723 ppm, with decreasing paramagnetic shift as *z* decreases and the samples become less defective. The observation of this signal is consistent with previous findings.[13,44] It is caused by transfer of unpaired electron spin density from Ni^{3+} to Li^+ via six 90° and six 180° oxygen-bridged bonds from 12 surrounding nickel ions.[13,45,46] A shoulder peak appears at ~850 ppm with increasing Li off-stoichiometry (see **Figure 2b**), which has been attributed previously to an intrinsic anisotropy of the NMR signal of LNO.[13] However, this apparent anisotropy is not visible in the spectrum of IE-LNO. Therefore, we assign it to Ni^{2+} states,[47] present for charge neutrality reasons (formation of two Ni^{2+}, on the defect site and in the Ni layer). The defects interact with lithium via a 90° oxygen-bridged bond.[48] With decreasing Li off-stoichiometry, the shoulder peak diminishes in intensity, while the main paramagnetic peak becomes more prominent and shifts to lower ppm. In the extreme case of IE-LNO, it is not observed, which is in good agreement with the XRD data, indicating the lack of (nickel) substitutional defects, as expected for “perfectly” layered LNO. A second peak is detected at ~460 ppm. A lower chemical shift should be caused by a less paramagnetic Li^+ environment. Interestingly, the peak intensity increases with decreasing Li off-stoichiometry in the SS-LNO reference samples or, in other words, with increasing lithium excess in the synthesis, but it is not observed for IE-LNO. The signal could be related to the presence of Ni^{4+}, due to formation of slightly overlithiated SS-LNO. In this case, lithium atoms would occupy the Ni site and induce the formation of Ni^{4+} for charge balancing. The appearance of the peak could also be caused by lithium-containing NiO with a rocksalt-type structure. Additional peaks in the range from 200 to 400 ppm have been assigned to Li^+ in the Ni layer by Bianchini *et al.*[45]

The structural information obtained from ^{7}Li MAS NMR spectroscopy, represented by the narrow peak at 720 ppm and the absence of additional peaks, hints at a uniform magnetic environment in IE-LNO. This agrees with our hypothesis of “perfect” layering achieved by low-temperature ion-exchange synthesis. The Li slabs may still contain a few percent of Na^+ ions, as found by Rietveld refinement. However, they do not induce paramagnetic shifts in the Li^+ environment. Furthermore, the structural information presented here is limited to the close proximity of lithium and therefore does not account for the presence of impurity phases, such as NiO. Nevertheless, considering only the main phase, we can conclude that no Ni^{2+} ions are occupying the crystallographic Li site.

^{23}Na NMR spectroscopy measurements were conducted on the IE-LNO and NNO-600 samples to probe the presence of Na^+ ions in the layered structure after ion exchange. The corresponding spectra are shown in **Figure 2c**. The most intense peak in the NNO-600 spectrum is observed at ~1400 ppm, stemming from Na^+ in the NNO structure. The 12 surrounding Ni^{3+} ions interact with sodium and cause a paramagnetic shift through 90° and 180° oxygen-bridged bonds. A second peak is visible around 0 ppm, which can be attributed to Na residues that are not part of the NNO structure. This signal is most likely caused by unreacted NaOH (note that *n*(Ni):*n*(Na) = 1:1.1 in

the synthesis). After ion exchange, the main peak is located at 0 ppm, corresponding to the presence of Na-containing impurities, such as $NaNO_3$. A broad peak appears between 1400 and 1600 ppm, as can be seen in **Figure 2d**. After background subtraction and peak integration, the signal is found to be ~4.2% relative to NNO-600. Because it shows a paramagnetic shift, we assume this amount of Na^+ to be present in the Li layer of IE-LNO. The complementary results from XRD and elemental analysis thus lead to the conclusion that ~5% Na^+ ions are left in the structure after the first ion-exchange step.

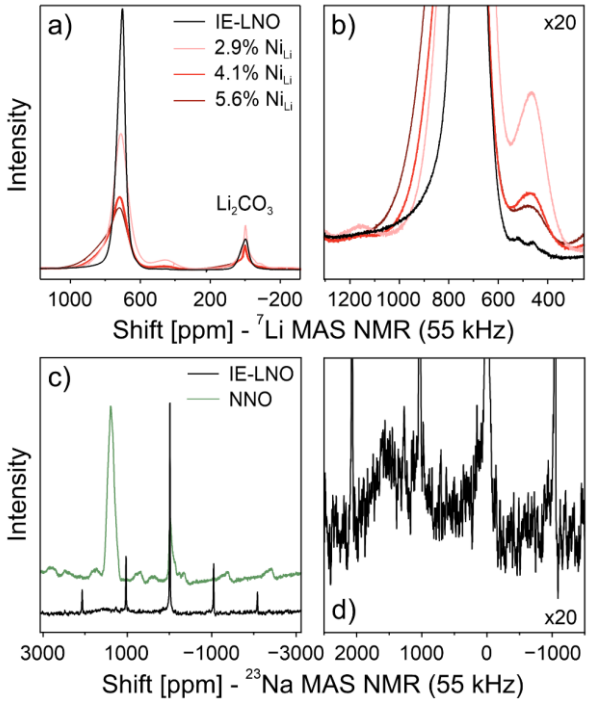

Figure 2. a) ^{7}Li MAS NMR spectra of LNO-set1 (red) and IE-LNO (black). b) Zoomed-in region of interest. c) ^{23}Na MAS NMR spectra collected prior to (green) and after ion exchange (black). d) Zoomed-in region of interest for IE-LNO.

Particle Size Control and Microstructure

While point defects determine properties at the atomic level, it is also important to understand the effect that microstructure and particle morphology (on the nm to µm scale) have in general. In addition to improvements in the degree of layering over the SS-LNO sample, the synthesis procedure employed in the present work allows for the preparation of monolithic particles of controlled size. The ion-exchange reaction proceeds in a topotactic manner, leading to the formation of intact (non-agglomerated) monolithic grains, as highlighted in **Figure 3a**. The particle size distribution was analyzed via scanning electron microscopy (SEM) image processing (see Supporting Information for details). The equivalent diameter d_{eq} of ion-exchanged samples from NNO prepared at different temperatures (6 h) increased by about an order of magnitude from ~0.4 µm for 450 °C to ~3.6 µm for 700 °C (d_{50}, see **Figure 3b**). This corresponds to an increase in mass and volume per particle by a factor of ~500. As can be seen, the particle size distribution is multimodal, which may help to increase

packing density (tap density). The correlation between the particle size distribution of NNO-600 (12 h) and that of IE-LNO was also examined (see **Figure S3** for violin and box-plot analyses). A small increase in the d_{eq} of IE-LNO is evident from the data, which we attribute to selective removal of “small” particles during the washing step and the sampling size. Overall, the ion-exchange route allows for tailoring of the particle size from the typical primary particle level of polycrystalline CAMs to µm-sized single crystals. Contrary to conventional single-crystalline materials prepared via solid-state synthesis, minimal agglomeration of the individual particles/grains is observed after ion exchange, rendering post deagglomeration procedures moot.

The morphology of the obtained LNO particles is largely inherited from the NNO precursor, as can be seen from **Figures 1b**-**e**, **3a**, and **S4**. Microstructural analysis via scanning transmission electron microscopy (STEM) imaging revealed microcracking throughout the particles and the presence of rocksalt-type NiO surrounding the cracks (see **Figure 1e**). The NiO domains are not visible in the XRD patterns (see **Figures 1a**, **f**, and **3c**), suggesting a low mass fraction of ≤ 1 - 2 wt. %. Comparing the change in microstructure from NNO to IE-LNO, the crack formation appears to be a result of the ion-exchange reaction itself. We expect it to negatively impact the cycling performance by hindering lithium diffusion. The surface of the water-washed IE-LNO was probed using electron energy loss spectroscopy (EELS, see **Figure S5**). EELS mapping revealed a two-layer structure of ~12 nm thickness, with the top layer containing primarily Ni^{2+} ions. The layer underneath shows mixed oxidation states (2+/3+) for Ni (similar observations are made for cracks), probably owing to the ion-exchange and washing procedures.

The size distribution, microstructure, and shape of the particles are the results of a complex interplay between processes occurring during NNO synthesis, Na^+/Li^+ exchange, and subsequent washing, all of which potentially affects the electrochemical performance of the LNO CAM.

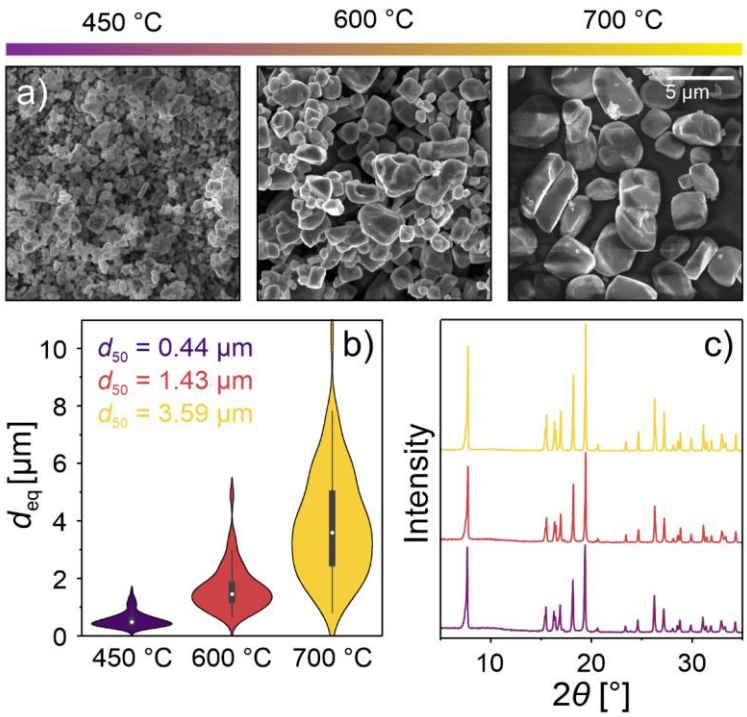

Figure 3. a) SEM images of IE-LNO particles derived from NNO prepared at temperatures of 450, 600, and 700 °C (6 h). b) Corresponding particle size distributions and c) XRD patterns (see **Table 1** for Rietveld refinement results).

Kinetic Pathway of Na^+/Li^+ Exchange

To better understand the kinetics of the ion-exchange reaction, *in situ* XRD data were collected during heating of a mixture of NNO-600 and $LiNO_3$, see contour plot in **Figure 4**. Initially, the reflections can be indexed to NNO and $LiNO_3$. At ~140 °C, those of $LiNO_3$ start to decrease in intensity, while a weak $NaNO_3$ signal is detected, which increases with increasing temperature. At ~180 °C, the background becomes diffuse (with increasing intensity) and the reflections of $LiNO_3$ and $NaNO_3$ disappear. This could be indicative of the formation of a liquid $LiNO_3$:$NaNO_3$ eutectic, which has a melting point of ~190 °C.[49] The NNO reflections start to decrease in intensity at 170 °C, suggesting the onset of a reaction below the melting point of $LiNO_3$. A second peak at lower diffraction angles is observed in the temperature range from 150 to 230 °C, herein denoted as NNO'. This peak probably stems from a Na-deficient (oxidized) structure, as is known for chemical deintercalation of Na^+ from NNO materials.[28] The formation of layered LNO occurs at ~190 °C, evident from the presence of broad reflections that become narrower with increasing temperature (their intensity continues to increase until the temperature of the mixture reaches 260 °C). These findings point to a (complex) multistep reaction: (i) 140 °C ≤ ϑ ≤ 170 °C: oxidation of NNO toward NNO' accompanied by Na^+/Li^+ ion migration; (ii) 170 °C < ϑ ≤ 210 °C: formation of LNO via the NNO → NNO' pathway in an eutectic melt of $LiNO_3$:$NaNO_3$; (iii) 210 °C < ϑ ≤ 230 °C: disappearance of the NNO (full conversion) and LNO crystallization; and (iv)

ϑ > 230 °C: disappearance of the NNO', further crystallization of LNO, and solidification of the nitrate salt melt.

Taken together, the *in situ* XRD results indicate a fast and atomically efficient mechanism for the ion exchange with $LiNO_3$. Notably, the reaction yields single-phase LNO, even when using a relatively small excess of $LiNO_3$ (here, *n*($LiNO_3$):*n*(NNO) = 1.2:1).

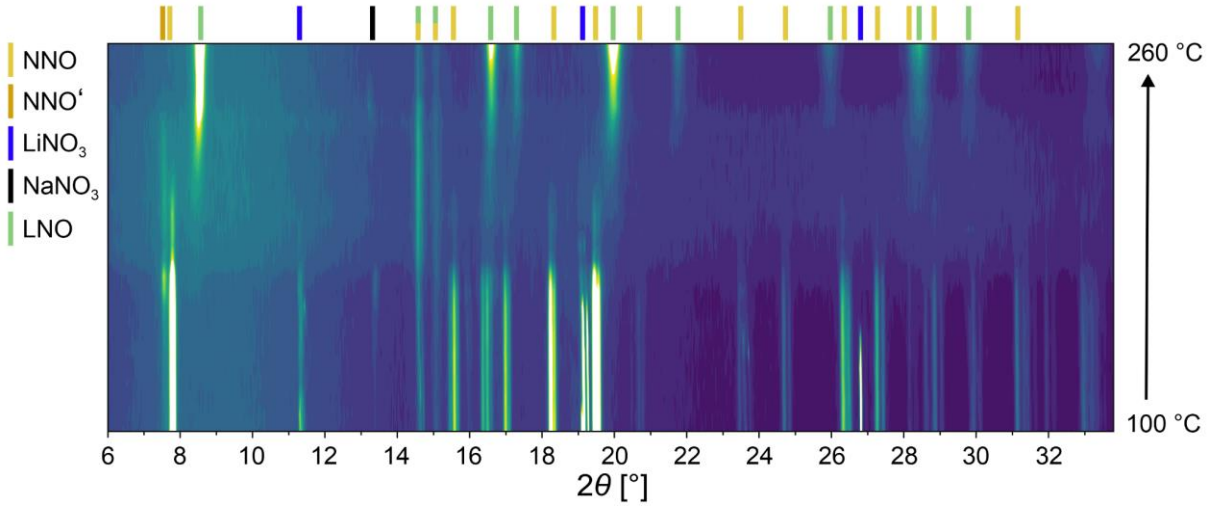

Figure 4. Contour plot of *in situ* XRD data collected during heating of a 1:1 wt. mixture of NNO-600 and $LiNO_3$ in an O_2 atmosphere at 1 K min^{-1}.

Electrochemistry and *Operando* XRD

To investigate the electrochemical behavior and the structural changes during cycling, the CAMs were incorporated into electrodes and cycled against Li metal in coin cells in the potential range between 3.0 and 4.3 V vs. Li^+/Li. Interestingly, the voltage profiles differ to some degree from the charge/discharge curves observed for SS-LNO, see **Figure 5a**, **b**. The choice of exchange salt/washing solvent is found to have a strong effect on the capacity, with the best results achieved for $LiNO_3/H_2O$ (see **Figure S2**). Thus, in the following, the cycling performance of the latter IE-LNO is compared to that of the SS-LNO reference CAM with a relatively low Li off-stoichiometry (1.7(2)% $Ni_{Li}^{\bullet}$). However, the positions of the phase transitions are similar for all ion-exchanged materials. This is indicative of the same structure for the electrochemically active fraction of CAMs, with similar electrochemical behavior of the bulk material (independent of the synthesis/post-processing conditions). The residual Na is apparently not playing a major role. Note that Na-doped SS-LNO cathodes show the same d*q*/d*V* peaks as the SS-LNO sample (see **Figure S2**).[25,43] The specific discharge capacity increases from ~173 to ~185 mAh g^{-1} (~1.3 mAh cm^{-2}) over the first 5 cycles at 0.1C rate, which is probably related to opening of pores. A similar effect is observed for the SS-LNO reference CAM (see **Figure 5c**). However, the latter material is capable of delivering capacities that are larger by up to 40 mAh g^{-1}. As expected, the fading is somewhat lower for the IE-LNO, with specific discharge capacities of ~161 and

~151 mAh g^{-1} at 0.1C for SS-LNO and IE-LNO, respectively, after 100 additional cycles at 0.5C charge and 1C discharge (plus a 0.1C testing after 55 cycles).

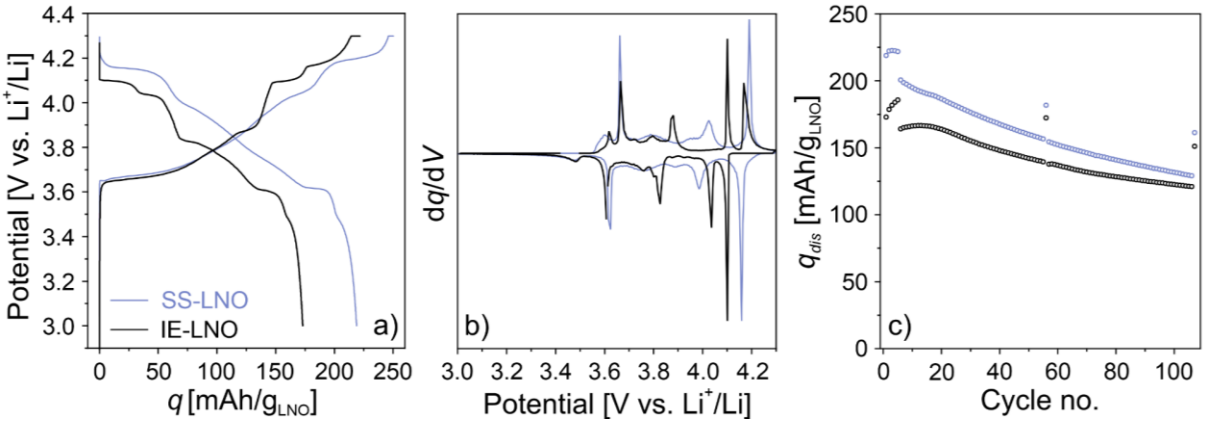

Figure 5. a) Initial-cycle charge/discharge curves, b) second-cycle differential capacity curves, and c) capacity retention for water-washed IE-LNO (black) and SS-LNO (blue). The first five cycles were performed at a rate of 0.1C, followed by 0.5C charge and 1C discharge cycling (0.1C after 55 and 106 cycles).

During electrochemical delithiation, LNO is expected to undergo transitions between several hexagonal and monoclinic phases, commonly denoted as H1 ↔ M ↔ H2 ↔ H3. These transitions have been well characterized previously.[50–52] To examine whether the preparation of LNO via ion exchange affects the structural transitions, *operando* XRD was conducted on the IE-LNO. As discussed above, the CAM presents different features in the differential capacity curve compared to SS-LNO.[51] **Figure 6** shows the refined structural parameters for the initial cycle at C/30 rate (3.0 - 4.5 V vs. Li^+/Li) together with the potential. An example of the typical quality of fit is provided in **Figure S6**. An extended voltage window up to 4.5 V was used for *operando* XRD, whereas electrochemical testing was done with a cutoff potential of 4.3 V, resulting in overall slightly lower capacities, but higher cycling stability. In the experiment, the material delivered specific charge and discharge capacities of 215.9 and 201.5 mAh g^{-1}, respectively, and was found to transition through the expected phases upon delithiation. From OCV to ~3.7 V, the material retains the initial hexagonal structure (H1). Afterwards, it undergoes a transition toward the monoclinic phase (M1), which is characterized by the splitting of selected reflections; for example, the 101_h reflection splits into the $20\bar{1}_m$ and 110_m reflections, as can be seen in the 16.0° < 2θ < 16.8° region in **Figure S6**. The transition from M' to M'' is found as a peak in the differential capacity curve and can be tracked by two regions, in which a maximum difference between the *a* and *b* lattice parameters is observed. This behavior indicates full conversion to M' and M'', separated by a clear convergence of the two parameters at ~3.9 V. The transition back to hexagonal (H2) is observed at ~4.1 V, followed by the H2 to H3 phase transition at 4.2 V. During the monoclinic regime, the *c* lattice parameter increases gradually from 14.284(4) Å (~3.7 V) to a maximum of 14.604(3) Å (~4.07 V). Beyond 4.1 V, a small decrease is observed as the material transitions toward the H2 phase, with *c* = 14.552(9) Å at 4.2 V. The transition to the H3 phase

results in a drastic reduction, from ~14.552(9) Å to ~13.115(7) Å, the latter being much lower than typically reported for LNO.[51,52] The overall behavior is consistent with previous findings, suggesting that the exchange reaction does not adversely affect the structural evolution of the system. As the potential approaches 4.5 V, another peak appears in the differential capacity curve, which is not seen in the discharge curve. We attribute it to the H3 to H4 transition, which occurs upon full delithiation of LNO and apparently is only visible at very low current rates.[10] Since this phase transition is impeded by Li off-stoichiometry, preventing sheet gliding at 7%,[53,54] we expect it to be more pronounced in a sample with no substitutional defects, as there is no Ni^{2+} present in the Li slab. This observation agrees with the data described above.

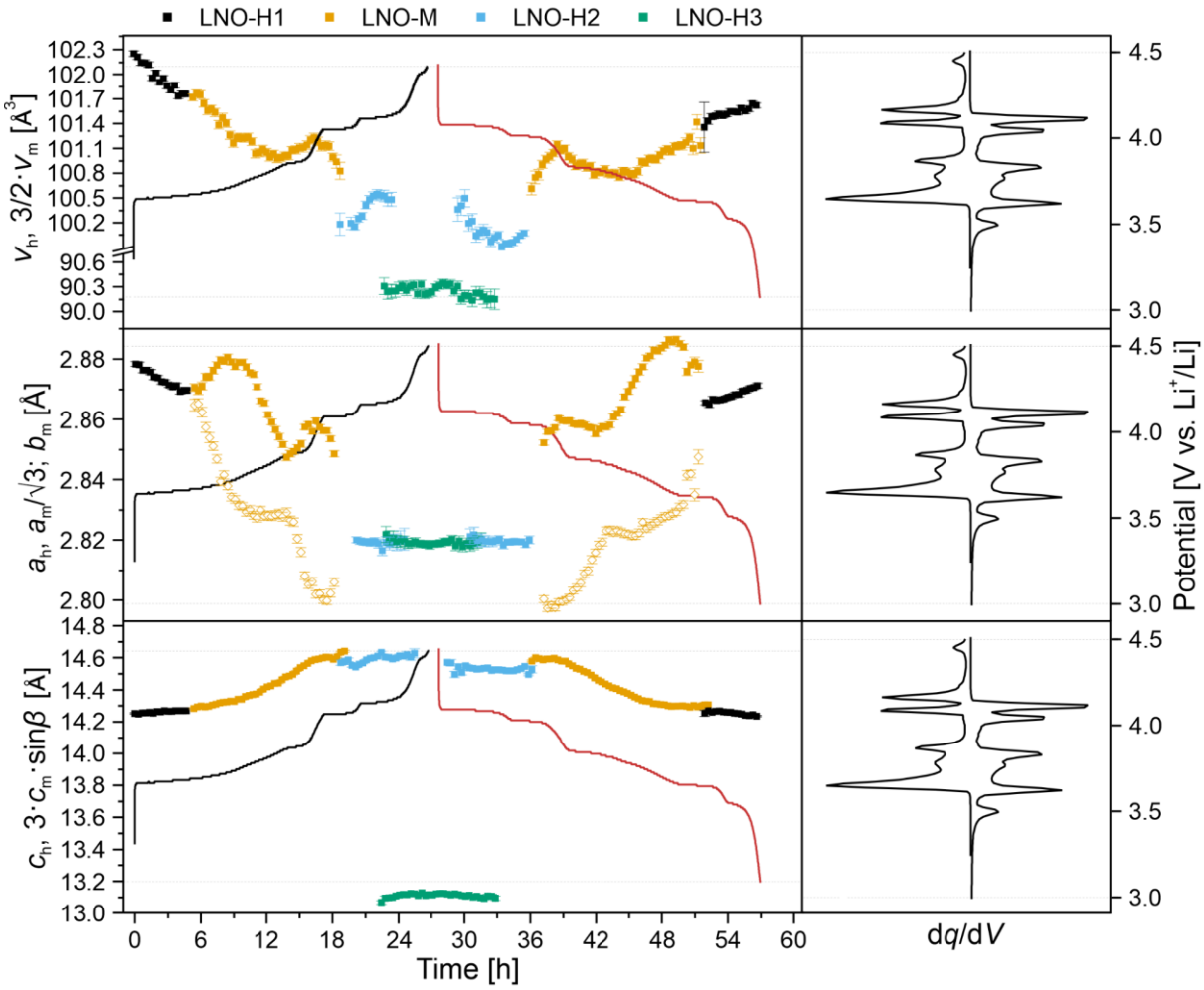

Figure 6. Refinement results for the lattice parameters and cell volume of the hexagonal (H) and monoclinic (M) phases. *Operando* XRD was conducted on the IE-LNO cathode in half-cells cycled at C/30 rate in the potential range 3.0 - 4.5 V vs. Li^+/Li.

The aforementioned phase transitions are typical of LNO CAMs, but the potential ranges at which they occur are somewhat shifted for the IE-LNO sample studied here. In general, the potential of the H2-H3 transition is found to shift to higher values with increasing Li off-stoichiometry.[12] This is caused by increasing destabilization of the H3 phase, due to Ni^{2+} occupying the Li site.[9] In **Figure 7**, the mean H2-H3 (peak) potential

for various IE-LNO CAMs is compared to that of the LNO-set1 reference samples (see Supporting Information for details on the d*q*/d*V* peak analysis). A linear regression was applied to the data in accordance with the procedure reported by Kurzhals and coworkers.[12] From this, the mean potential of the H2-H3 transition for "perfectly" layered LNO (0% $Ni_{Li}^{\bullet}$) is estimated at 4.138(5) V vs. Li^+/Li. The results of Kurzhals *et al*. are also reproduced in **Figure 7** (referred to as LNO-set2). From the analysis of these data, a potential of 4.148(3) V is determined. As can be seen, both datasets follow a linear relationship but are slightly offset with respect to each other. The reason is likely a systematic error in the determination of the Li off-stoichiometry by XRD. We attribute the H2-H3 transition potential of 4.13 - 4.15 V to the lack of off-stoichiometry and therefore intrinsic stabilization of the H3 phase (i.e. the absence of nickel substitutional defects strongly affects the mean potential of the phase transitions).

Taken together, the structural information from ^{7}Li MAS NMR spectroscopy agrees well with the empirical electrochemical evidence, indicating high ordering of the ion-exchanged LNO. However, the specific capacity delivered by the obtained material is lower than that of the reference material. We believe the main reasons for this are the formation of cracks and rocksalt-type NiO domains during ion exchange. An additional annealing step in the presence of a lithium source might help to produce a high-capacity material. An alternative strategy could be doping of the parent NNO compound for increasing structural integrity in the exchange reaction. Lastly, we consider coating of the particles an interesting approach to prevent unwanted surface side reactions with the washing solvent.

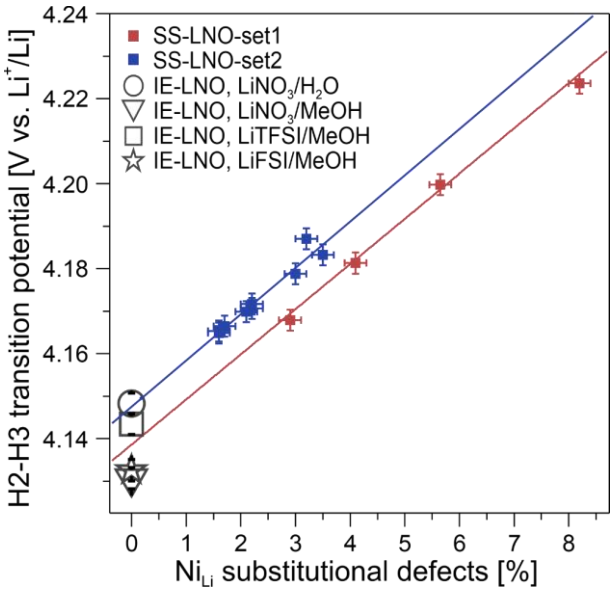

Figure 7. H2-H3 transition potential for LNO-set1, LNO-set2, and various IE-LNO samples from differential capacity curves as a function of the Li off-stoichiometry (from XRD for LNO-set1 and LNO-set2). The peak potentials shown are average values from charge and discharge.

Conclusion

In summary, we have successfully developed a novel two-step calcination process followed by facile ion exchange for the preparation of LNO single crystals. The layered structure of the parent NNO phase is maintained during Na^+/Li^+ exchange, leading to a material that is free of Ni^{2+} substitutional defects on the Li site. This is confirmed by XRD and solid-state NMR spectroscopy measurements, the latter indicating a very uniform Li^+ environment. The synthesis procedure further allows for size tailoring of the monolithic LNO grains. The absence of $Ni_{Li}^{\bullet}$ point defects is found to directly affect the charge/discharge behavior of ion-exchanged LNO by altering the voltage at which the characteristic phase transitions occur. The changes are neither associated with electrochemical reactivity to a specific lithium salt used for ion exchange or washing solvent nor residual Na present in the structure. We believe that this methodology, once optimized for battery performance by suppressing NiO formation and cracking, among others, is applicable to study size effects in LNO (fracture behavior, charge-storage kinetics, interfacial degradation, etc.) and related single-crystalline materials and may help to better understand the electrochemical implications of Li off-stoichiometry in layered oxide cathodes.

Experimental Section

Materials Synthesis

$NaNiO_2$ was synthesized by solid-state reaction from $Ni(OH)_2$ (d_{50} ≈ 4 µm, BASF SE) and NaOH (Sigma-Aldrich). The reactants were homogenized under Ar atmosphere for 5 min with 10 mol % excess of NaOH, i.e. *n*(Ni):*n*(Na) = 1:1.1, using a laboratory blender (Kinematica). The blended precursor mixture was heated in an alumina crucible under O_2 flow (2 atm h^{-1}) in a tube furnace (Nabertherm P330) at 300 °C for 10 h with 3 K min^{-1} heating and cooling rates. After cooling to room temperature, it was homogenized again for 5 min and the resulting mixture transferred to an alumina crucible for calcination at temperatures ranging from 450 to 700 °C for 6 - 12 h using the above-mentioned conditions.

$LiNiO_2$ was synthesized via ion exchange by mixing $NaNiO_2$ with 20 mol % excess of $LiNO_3$ and heating to 320 °C under Ar atmosphere. After cooling to room temperature, the mixture was washed twice with water under stirring. The resulting powder was dried in a vacuum at 120 °C (see Supporting Information for water-free washing procedures and alternative lithium salts for ion exchange).

Electrochemical Testing

Electrodes were prepared by casting an *N*-methyl-pyrrolidone (NMP)-based slurry with 94 wt. % CAM, 3 wt. % Super C65 carbon, and 3 wt. % polyvinylidene difluoride (PVDF, Solef 5130; Solvay) onto an Al foil current collector. The slurry was prepared by combining all constituents with 20 wt. % additional NMP in a planetary centrifuge mixer (ARE250, Thinky) and stirring applying a two-step program (3 min at 2000 rpm, 3 min at 400 rpm). The slurry was spread onto 0.03 mm Al foil using an Erichsen

Coatmaster 510 film applicator at a rate of 5 mm s^{-1}. The as-made tapes were dried overnight in a vacuum at 120 °C and then calendered at 14 N mm^{-1} (Sumet Messtechnik). Cathodes of 13 mm diameter and 7 - 10 mg_{CAM} cm^{-2} areal loading were punched out, and half-cells with LP57 electrolyte (1 M $LiPF_6$ in a 3:7 weight ratio mixture of ethylene and ethyl methyl carbonate), GF/D separator, and Li metal assembled in an Ar glovebox. Electrochemical testing was done in the potential range of 3.0 - 4.3 V vs. Li^+/Li. The first five cycles were carried out at a rate of 0.1C (1C = 220 mA g^{-1}), followed by 100 cycles at 0.5C charge and 1C discharge (0.1C after 55 and 106 cycles), with constant voltage charging until the specific current decayed to 0.02C.

X-ray Diffraction

XRD patterns were collected on a STADI P (STOE) diffractometer in Debye-Scherrer geometry utilizing monochromatic Mo-Kα1 radiation (λ = 0.7093 Å, 50 kV, 40 mA) and a Mythen 1K detector (Dectris). The diffraction data sets were analyzed using TOPAS Academic v7. A LeBail fit was performed first, in which background correction was done by applying a Chebyshev polynomial function with 10 terms. Lattice parameters, zero-shift, axial divergence, and crystallite size were extracted as Gaussian and Lorentzian contributions. The phenomenological model by Stephens was used to refine *hkl*-dependent microstrain.[55] During Rietveld refinement, the parameters from the LeBail fit were first fixed, and the oxygen coordinate(s) z_O (LNO) and z_{O_1} and z_{O_2} (NNO), site occupancies, and Debye-Waller factors were refined while applying an absorption correction. Lastly, all parameters were refined in parallel until convergence was achieved. The confidence intervals are three times the estimated standard deviations as obtained from TOPAS Academic v7. The errors of cell volumes were estimated to be higher than the errors obtained directly from refinement and therefore rounded to the first significant digit after the comma when given in $Å^3$.

***Operando* XRD**

The positive caps, negative caps, and spacers of the coin-cell casings were modified by electro-erosion for *operando* XRD experiments to have a central hole of 5 mm diameter and sealed with glass windows of 6 mm diameter and 160 µm thickness using a surface-treated polyethylene foil. Cells were cycled at a rate of C/30 using a Gamry Interface 1000 potentiostat, while XRD patterns were collected simultaneously using a STOE Stadi-P diffractometer with a Mo anode. Diffraction data were collected in the range of $5° < 2\theta < 37°$ with a collection time of 21 min per pattern. Rietveld refinement was carried out sequentially on the diffraction data using GSAS-II.[56] The zero offset and instrumental contribution to peak broadening were determined by measurement of a LaB_6 660b reference material.

***In situ* XRD**

The exchange reaction was studied by *in situ* XRD using a custom-built diffractometer, the specifics of which were reported previously.[57] For sample preparation, a 1:1 wt. mixture of NNO-600 and $LiNO_3$ was ground in a mortar and filled into a sapphire capillary. The mixture was then heated at a rate of 1 K min^{-1} under O_2 atmosphere, with each XRD pattern being the accumulated signal over 5 min. Temperature

calibration was done by comparison with the cell volume of Al_2O_3 powder, which was measured in a separate heating experiment.

^{7}Li and ^{23}Na Nuclear Magnetic Resonance Spectroscopy

^{7}Li and ^{23}Na MAS NMR experiments were conducted on a Bruker Avance 200 MHz spectrometer at a magnetic field of 4.7 T. Spectra were acquired at a Larmor frequency of 77.8 MHz and 52.9 MHz for ^{7}Li and ^{23}Na, respectively, with 1.3 mm rotors and spinning at 55 kHz. A rotor-synchronized Hahn-echo pulse sequence (90°-τ-180°-τ-acquisition) was used, with a recycle delay of 1 s and 90° pulse lengths of 0.85 µs for ^{7}Li and 0.80 µs for ^{23}Na. The NMR shifts were referenced using aqueous 1 M LiCl and NaCl solutions (0 ppm). All spectra are normalized with respect to sample mass and number of scans.

Inductively Coupled Plasma-Optical Emission Spectroscopy

The elemental composition was determined by ICP-OES using a Thermo Fischer Scientific ICAP 7600 DUO. Powder samples were dissolved in an acid digester in a graphite furnace. The mass fraction values were obtained from three independent measurements for each sample. About 10 mg was dissolved in 6 mL hydrochloric acid and 2 mL nitric acid at 353 K for 4 h. The digested samples were diluted, and analysis of elements was conducted with four different calibration solutions and an internal standard (Sc). Two/three wavelengths of elements were used. The O content was analyzed by carrier gas hot extraction (CGHE) using a commercial oxygen/nitrogen analyzer TC600 (LECO). It was calibrated using the certified standard KED 1025 (ALPHA). The measurements were conducted at 5800 W.

Electron Microscopy

Morphological and compositional information about the as-prepared samples were obtained from field-emission SEM and EDX using a LEO-1530 microscope (Carl Zeiss AG). Specimen for TEM investigation were prepared by the lift-out technique using a Ga FIB on a STRATA dual-beam system. They were milled at 30 kV, followed by final polishing at 2 kV to reduce surface damage. Sample preparation was immediately followed by TEM investigation to reduce the risk of oxidation during storage and handling. TEM was performed on a Themis Z (Thermo Fisher Scientific) double-corrected transmission electron microscope at 300 kV. STEM images were collected using a HAADF detector. EELS data were acquired with an energy resolution of ~1 eV. Spectra were collected in dual EELS mode, allowing to lock the ZLP and use it as reference for accurate determination of the edge position for each element. Analysis was done out using the MLLS fitting method integrated in Gatan Digital Micrograph.

Associated Content

Supporting Information

The Supporting Information is available free of charge on the ACS Publication website at DOI:

Experimental section including synthesis of reference materials and details on alternative ion-exchange procedures, structural characterization from XRD and Rietveld refinement, particle size analysis, ICP-OES results, and additional data from electrochemical cycling and TEM analysis.

Author Information

Corresponding Authors

Daniel Weber – Battery and Electrochemistry Laboratory (BELLA), Institute of Nanotechnology, Karlsruhe Institute of Technology (KIT), Herrmann-von-Helmholtz-Platz 1, 76344 Eggenstein-Leopoldshafen, Germany and Institute for Applied Materials-Energy Storage Systems (IAM-ESS), Karlsruhe Institute of Technology (KIT), Herrmann-von-Helmholtz-Platz 1, 76344 Eggenstein-Leopoldshafen, Germany

Email: daniel.weber3@kit.edu

Jürgen Janek – Battery and Electrochemistry Laboratory (BELLA), Institute of Nanotechnology, Karlsruhe Institute of Technology (KIT), Herrmann-von-Helmholtz-Platz 1, 76344 Eggenstein-Leopoldshafen, Germany and Institute of Physical Chermistry & Center for Materials Research (ZfM/LaMa), Justus-Liebig-University Giessen, Heinrich-Buff-Ring 17, 35392 Giessen, Germany

Email: juergen.janek@phys.chemie.uni-giessen.de

Torsten Brezesinski – Battery and Electrochemistry Laboratory (BELLA), Institute of Nanotechnology, Karlsruhe Institute of Technology (KIT), Herrmann-von-Helmholtz-Platz 1, 76344 Eggenstein-Leopoldshafen, Germany

Email: torsten.brezesinski@kit.edu

Notes

The authors declare no competing financial interest.

Acknowledgements

This work was partially supported by the BASF SE. Thomas Bergfeldt is acknowledged for conducting the ICP-OES analysis and Svetlana Korneychuk and Philipp Müller for TEM analysis of IE-LNO and NNO, respectively. We thank Nikolai Bartnick and Holger Geßwein for experimental support as well as Philipp Kurzhals and Felix Riewald for sharing electrochemical data on LNO, denoted as LNO-set2 herein. We are also grateful to Marie Duffiet and Matteo Bianchini for helpful discussions regarding NMR spectroscopy and Na-doping of LNO.

References

(1) Nitta, N.; Wu, F.; Lee, J. T.; Yushin, G. Li-Ion Battery Materials: Present and Future. *Mater. Today* **2015**, *18*, 252–264.

(2) Blomgren, G. E. The Development and Future of Lithium Ion Batteries. *J. Electrochem. Soc.* **2017**, *164*, A5019–A5025.

(3) Noh, H.-J.; Youn, S.; Yoon, C. S.; Sun, Y.-K. Comparison of the Structural and Electrochemical Properties of Layered $Li[Ni_xCo_yMn_z]O_2$ (x = 1/3, 0.5, 0.6, 0.7, 0.8 and 0.85) Cathode Material for Lithium-Ion Batteries. *J. Power Sources* **2013**, *233*, 121–130.

(4) Kim, J.-H.; Ryu, H.-H.; Kim, S. J.; Yoon, C. S.; Sun, Y.-K. Degradation Mechanism of Highly Ni-Rich $Li[Ni_xCo_yMn_{1-x-y}]O_2$ Cathodes with x > 0.9. *ACS Appl. Mater. Interfaces* **2019**, *11*, 30936–30942.

(5) Li, W.; Reimers, J. N.; Dahn, J. R. Crystal Structure of $Li_xNi_{2-x}O_2$ and a Lattice-Gas Model for the Order-Disorder Transition. *Phys. Rev. B* **1992**, *46*, 3236–3246.

(6) Reimers, J. N.; Li, W.; Dahn, J. R. Short-Range Cation Ordering in $Li_xNi_{2-x}O_2$. *Phys. Rev. B* **1993**, *47*, 8486–8493.

(7) Bianchini, M.; Fauth, F.; Hartmann, P.; Brezesinski, T.; Janek, J. An In Situ Structural Study on the Synthesis and Decomposition of $LiNiO_2$. *J. Mater. Chem. A* **2020**, *8*, 1808–1820.

(8) Lin, S. P.; Fung, K. Z.; Hon, Y. M.; Hon, M. H. Crystallization Kinetics and Mechanism of the $Li_xNi_{2-x}O_2$ ($0<x\leq1$) from Li_2CO_3 and NiO. *J. Cryst. Growth* **2002**, *234*, 176–183.

(9) Riewald, F.; Kurzhals, P.; Bianchini, M.; Sommer, H.; Janek, J.; Gasteiger, H. A. The $LiNiO_2$ Cathode Active Material: A Comprehensive Study of Calcination Conditions and Their Correlation with Physicochemical Properties Part II. Morphology. *J. Electrochem. Soc.* **2022**, *169*, 020529.

(10) Bianchini, M.; Roca-Ayats, M.; Hartmann, P.; Brezesinski, T.; Janek, J. There and Back Again—The Journey of $LiNiO_2$ as a Cathode Active Material. *Angew. Chem. Int. Ed.* **2019**, *58*, 10434–10458.

(11) Shannon, R. D. Revised Effective Ionic Radii and Systematic Studies of Interatomie Distances in Halides and Chaleogenides. *Acta Crystallogr.* **1976**, *A32*, 751–767.

(12) Kurzhals, P.; Riewald, F.; Bianchini, M.; Sommer, H.; Gasteiger, H. A.; Janek, J. The $LiNiO_2$ Cathode Active Material: A Comprehensive Study of Calcination Conditions and Their Correlation with Physicochemical Properties. Part I. Structural Chemistry. *J. Electrochem. Soc.* **2021**, *168*, 110518.

(13) Chazel, C.; Ménétrier, M.; Croguennec, L.; Delmas, C. $^{6/7}$Li NMR Study of the $Li_{1-z}Ni_{1+z}O_2$ Phases. *Magn. Reson. Chem.* **2005**, *43*, 849–857.

(14) Rougier, A.; Gravereau, P.; Delmas, C. Optimization of the Composition of the $Li_{1-z}Ni_{1+z}O_2$ Electrode Materials: Structural, Magnetic, and Electrochemical Studies. *J. Electrochem. Soc.* **1996**, *143*, 1168–1175.

(15) Pouillerie, C.; Croguennec, L.; Biensan, Ph.; Willmann, P.; Delmas, C. Synthesis and Characterization of New $LiNi_{1-y}Mg_yO_2$ Positive Electrode Materials for Lithium-Ion Batteries. *J. Electrochem. Soc.* **2000**, *147*, 2061–2069.

(16) Weber, D.; Lin, J.; Pokle, A.; Volz, K.; Janek, J.; Brezesinski, T.; Bianchini, M. Tracing Low Amounts of Mg in the Doped Cathode Active Material $LiNiO_2$. *J. Electrochem. Soc.* **2022**, *169*, 030540.

(17) Yabuuchi, N.; Ohzuku, T. Novel Lithium Insertion Material of $LiCo_{1/3}Ni_{1/3}Mn_{1/3}O_2$ for Advanced Lithium-Ion Batteries. *J. Power Sources* **2003**, *119–121*, 171–174.

(18) MacNeil, D. D.; Lu, Z.; Dahn, J. R. Structure and Electrochemistry of $Li[Ni_xCo_{1-2x}Mn_x]O_2$ ($0 \leq x \leq 1/2$). *J. Electrochem. Soc.* **2002**, *149*, A1332–A1336.

(19) Amatucci, G. G.; Tarascon, J.-M.; Larcher, D.; Klein, L. C. Synthesis of Electrochemically Active $LiCoO_2$ and $LiNiO_2$ at 100 °C. *Solid State Ionics* **1996**, *84*, 169–180.

(20) Palacin, M. R.; Larcher, D.; Audemer, A.; Sac-Epee, N.; Amatucci, G. G.; Tarascon, J.-M. Low-Temperature Synthesis of $LiNiO_2$: Reaction Mechanism, Stability, and Electrochemical Properties. *J. Electrochem. Soc.* **1997**, *144*, 4226–4236.

(21) Larcher, D.; Palacín, M. R.; Amatucci, G. G.; Tarascon, J. -M. Electrochemically Active $LiCoO_2$ and $LiNiO_2$ Made by Cationic Exchange under Hydrothermal Conditions. *J. Electrochem. Soc.* **1997**, *144*, 408–417.

(22) Pritzl, D.; Teufl, T.; Freiberg, A. T. S.; Strehle, B.; Sicklinger, J.; Sommer, H.; Hartmann, P.; Gasteiger, H. A. Editors' Choice—Washing of Nickel-Rich Cathode Materials for Lithium-Ion Batteries: Towards a Mechanistic Understanding. *J. Electrochem. Soc.* **2019**, *166*, A4056–A4066.

(23) Toma, T.; Maezono, R.; Hongo, K. Electrochemical Properties and Crystal Structure of Li^+/H^+ Cation-Exchanged $LiNiO_2$. *ACS Appl. Energy Mater.* **2020**, *3*, 4078–4087.

(24) Sun, Y.; Wan, P.; Pan, J.; Xu, C.; Liu, X. Low Temperature Synthesis of Layered $LiNiO_2$ Cathode Material in Air Atmosphere by Ion Exchange Reaction. *Solid State Ionics* **2006**, *177*, 1173–1177.

(25) Holzapfel, M.; Darie, C.; Bordet, P.; Chappel, E.; Núñez-Regueiro, M.-D.; Diaz, S.; de Brion, S.; Chouteau, G.; Strobel, P. Mixed Layered Oxide Phases $Na_xLi_{1-x}NiO_2$: A Detailed Description of Their Preparation and Structural and Magnetic Identification. *Solid State Sci.* **2005**, *7*, 497–506.

(26) Matsumura, T.; Kanno, R.; Gover, R.; Kawamoto, Y.; Kamiyama, T.; Mitchell, B. J. Synthesis, Structure and Physical Properties of $Li_xNa_{1-x}NiO_2$. *Solid State Ionics* **2002**, *152–153*, 303–309.

(27) Vassilaras, P.; Ma, X.; Li, X.; Ceder, G. Electrochemical Properties of Monoclinic $NaNiO_2$. *J. Electrochem. Soc.* **2013**, *160*, A207–A211.

(28) Han, M. H.; Gonzalo, E.; Casas-Cabanas, M.; Rojo, T. Structural Evolution and Electrochemistry of Monoclinic $NaNiO_2$ upon the First Cycling Process. *J. Power Sources* **2014**, *258*, 266–271.

(29) Dyer, L. D.; Borie Jr., B. S.; Smith, G. P. Alkali Metal-Nickel Oxides of the Type $MNiO_2$. *J. Am. Chem. Soc.* **1954**, *76*, 1499–1503.

(30) Wang, L.; Wang, J.; Zhang, X.; Ren, Y.; Zuo, P.; Yin, G.; Wang, J. Unravelling the Origin of Irreversible Capacity Loss in $NaNiO_2$ for High Voltage Sodium Ion Batteries. *Nano Energy* **2017**, *34*, 215–223.

(31) Chappel, E.; Núñez-Regueiro, M. D.; Dupont, F.; Chouteau, G.; Darie, C.; Sulpice, A. Antiferromagnetic Resonance and High Magnetic Field Properties of $NaNiO_2$. *Eur. Phys. J. B* **2000**, *17*, 609–614.

(32) Chappel, E.; Núñez-Regueiro, M. D.; Chouteau, G.; Isnard, O.; Darie, C. Study of the Ferrodistorsive Orbital Ordering in $NaNiO_2$ by Neutron Diffraction and Submillimeter Wave ESR. *Eur. Phys. J. B* **2000**, *17*, 615–622.

(33) Delmas, C.; Borthomieu, Y.; Faure, C.; Delahaye, A.; Figlarz, M. Nickel Hydroxide and Derived Phases Obtained by Chimie Douce from $NaNiO_2$. *Solid State Ionics* **1989**, *32–33*, 104–111.

(34) Tsuda, M.; Arai, H.; Takahashi, M.; Ohtsuka, H.; Sakurai, Y.; Sumitomo, K.; Kageshima, H. Electrode Performance of Layered $LiNi_{0.5}Ti_{0.5}O_2$ Prepared by Ion Exchange. *J. Power Sources* **2005**, *144*, 183–190.

(35) Cao, X.; Qiao, Y.; Jia, M.; He, P.; Zhou, H. Ion-Exchange: A Promising Strategy to Design Li-Rich and Li-Excess Layered Cathode Materials for Li-Ion Batteries. *Adv. Energy Mater.* **2022**, *12*, 2003972.

(36) Wu, E. J.; Tepesch, P. D.; Ceder, G. Size and Charge Effects on the Structural Stability of $LiMO_2$ (M = Transition Metal) Compounds. *Philos. Mag. B* **1998**, *77*, 1039–1047.

(37) Tournadre, F.; Croguennec, L.; Saadoune, I.; Carlier, D.; Shao-Horn, Y.; Willmann, P.; Delmas, C. On the Mechanism of the P2-$Na_{0.70}CoO_2$→O2- $LiCoO_2$ Exchange Reaction—Part I: Proposition of a Model to Describe the P2-O2 Transition. *J. Solid State Chem.* **2004**, *177*, 2790–2802.

(38) Kadoma, Y.; Oshitari, S.; Ui, K.; Kumagai, N. Synthesis of Hollandite-Type Li_xMnO_2 by Li^+ Ion-Exchange in Molten Salt and Lithium Insertion Characteristics. *Electrochim. Acta* **2007**, *53*, 1697–1702.

(39) Hua, W.; Wang, S.; Wang, K.; Missyul, A.; Fu, Q.; Dewi Darma, M. S.; Li, H.; Baran, V.; Liu, L.; Kübel, C.; Binder, J. R.; Knapp, M.; Ehrenberg, H.; Indris, S. Li^+/Na^+ Ion Exchange in Layered $Na_{2/3}(Ni_{0.25}Mn_{0.75})O_2$: A Simple and Fast Way to Synthesize O3/O2-Type Layered Oxides. *Chem. Mater.* **2021**, *33*, 5606–5617.

(40) Luo, Y.-h.; Pan, Q.-l.; Wei, H.-x.; Huang, Y.-d.; Tang, L.-b.; Wang, Z.-y.; He, Z.-j.; Yan, C.; Mao, J.; Dai, K.-h.; Zhang, X.-h.; Zheng, J.-c. Towards Ni-Rich Layered Oxides Cathodes with Low Li/Ni Intermixing by Mild Molten-Salt Ion Exchange for Lithium-Ion Batteries. *Nano Energy* **2022**, *102*, 107626.

(41) Kang, B.; Ceder, G. Battery Materials for Ultrafast Charging and Discharging. *Nature* **2009**, *458*, 190–193.

(42) Kang, K.; Meng, Y. S.; Bréger, J.; Grey, C. P.; Ceder, G. Electrodes with High Power and High Capacity for Rechargeable Lithium Batteries. *Science* **2006**, *311*, 977–981.

(43) Kim, H.; Choi, A.; Doo, S. W.; Lim, J.; Kim, Y.; Lee, K. T. Role of Na^+ in the Cation Disorder of $[Li_{1-x}Na_x]NiO_2$ as a Cathode for Lithium-Ion Batteries. *J. Electrochem. Soc.* **2018**, *165*, A201–A205.

(44) Li, H.; Hua, W.; Liu-Théato, X.; Fu, Q.; Desmau, M.; Missyul, A.; Knapp, M.; Ehrenberg, H.; Indris, S. New Insights into Lithium Hopping and Ordering in $LiNiO_2$ Cathodes during Li (De)Intercalation. *Chem. Mater.* **2021**, *33*, 9546–9559.

(45) Bianchini, M.; Schiele, A.; Schweidler, S.; Sicolo, S.; Fauth, F.; Suard, E.; Indris, S.; Mazilkin, A.; Nagel, P.; Schuppler, S.; Merz, M.; Hartmann, P.; Brezesinski, T.; Janek, J. From $LiNiO_2$ to Li_2NiO_3: Synthesis, Structures and Electrochemical Mechanisms in Li-Rich Nickel Oxides. *Chem. Mater.* **2020**, *32*, 9211–9227.

(46) Grey, C. P.; Dupré, N. NMR Studies of Cathode Materials for Lithium-Ion Rechargeable Batteries. *Chem. Rev.* **2004**, *104*, 4493–4512.

(47) Li, H.; Hua, W.; Schwarz, B.; Etter, M.; Mangold, S.; Melinte, G.; Casati, N. P. M.; Ehrenberg, H.; Indris, S. Investigation of Structural and Electronic Changes Induced by Postsynthesis Thermal Treatment of $LiNiO_2$. *Chem. Mater.* **2022**, *34*, 8163–8177.

(48) Mä, K.; Reeves, P. J.; Xu, C.; Griffith, K. J.; Grey, C. P. Evolution of Structure and Lithium Dynamics in $LiNi_{0.8}Mn_{0.1}Co_{0.1}O_2$ (NMC811) Cathodes during Electrochemical Cycling. *Chem. Mater.* **2019**, *31*, 2545–2554.

(49) Maeso, M. J.; Largo, J. The Phase Diagrams of $LiNO_3$-$NaNO_3$ and $LiNO_3$-KNO_3: The Behaviour of Liquid Mixtures. *Thermochim. Acta* **1993**, *223*, 145–156.

(50) Delmas, C.; Pérès, J. P.; Rougier, A.; Demourgues, A.; Weill, F.; Chadwick, A.; Broussely, M.; Perton, F.; Biensan, Ph.; Willmann, P. On the Behavior of the Li_xNiO_2 System: An Electrochemical and Structural Overview. *J. Power Sources* **1997**, *68*, 120–125.

(51) Li, H.; Zhang, N.; Li, J.; Dahn, J. R. Updating the Structure and Electrochemistry of Li_xNiO_2 for $0 \leq x \leq 1$. *J. Electrochem. Soc.* **2018**, *165*, A2985–A2993.

(52) de Biasi, L.; Schiele, A.; Roca-Ayats, M.; Garcia, G.; Brezesinski, T.; Hartmann, P.; Janek, J. Phase Transformation Behavior and Stability of $LiNiO_2$ Cathode Material for Li-Ion Batteries Obtained from In Situ Gas Analysis and Operando

X-Ray Diffraction. *ChemSusChem* **2019**, *12*, 2240–2250.

(53) Croguennec, L.; Pouillerie, C.; Delmas, C. Structural Characterisation of New Metastable NiO_2 Phases. *Solid State Ionics* **2000**, *135*, 259–266.

(54) Croguennec, L.; Pouillerie, C.; Mansour, A. N.; Delmas, C. Structural Characterisation of the Highly Deintercalated $Li_xNi_{1.02}O_2$ Phases (with $x \leq 0.30$). *J. Mater. Chem.* **2001**, *11*, 131–141.

(55) Stephens, P. W. Phenomenological Model of Anisotropic Peak Broadening in Powder Diffraction. *J. Appl. Cryst.* **1999**, *32*, 281–289.

(56) Toby, B. H.; Von Dreele, R. B. GSAS-II: The Genesis of a Modern Open-Source All Purpose Crystallography Software Package. *J. Appl. Cryst.* **2013**, *46*, 544–549.

(57) Geßwein, H.; Stüble, P.; Weber, D.; Binder, J. R.; Mönig, R. A Multipurpose Laboratory Diffractometer for Operando Powder X-Ray Diffraction Investigations of Energy Materials. *J. Appl. Cryst.* **2022**, *55*, 503–514.

TOC Graphic